

EFFECT OF SHEAR DEFORMATION AND CONTINUITY ON DELAMINATION MODELING WITH PLATE ELEMENTS

E.H. Glaessgen*, W.T. Riddell*, and I.S. Raju†

NASA Langley Research Center, Hampton, VA 23681-0001, U.S.A.

Abstract

The effects of several critical assumptions and parameters on the computation of strain energy release rates for delamination and debond configurations modeled with plate elements have been quantified. The method of calculation is based on the virtual crack closure technique (VCCT), and models that model the upper and lower surface of the delamination or debond with two-dimensional (2D) plate elements rather than three-dimensional (3D) solid elements. The major advantages of the plate element modeling technique are a smaller model size and simpler geometric modeling. Specific issues that are discussed include: constraint of translational degrees of freedom, rotational degrees of freedom or both in the neighborhood of the crack tip; element order and assumed shear deformation; and continuity of material properties and section stiffness in the vicinity of the debond front. Where appropriate, the plate element analyses are compared with corresponding two-dimensional plane strain analyses.

Introduction

Skin-stiffener debonding is considered a critical failure mode for stiffened composite panels. Figure 1(a) shows the elements of a composite skin-stiffened panel including a detail of a flange-skin debond. Much of the research on skin-stiffener debonding failure has focused on the calculation of skin-stiffener interface stresses.¹⁻³ These interface stresses initiate debonds at the edges of the stiffening elements as shown in Figure 1(b). Fracture mechanics approaches utilizing the concept of strain energy release rate have been used to predict the growth of these types of skin-stiffener debonds with considerable success.⁴⁻⁶

Models based on quasi-3D (extruded 2D) or 3D brick finite elements have been used to study edge delamination and near-surface delamination of composites.⁴⁻⁶ Since many layers of brick elements

through the thickness are often required to model both the skin panel and the associated stiffeners, the size of finite element models required for accurate analyses may become prohibitively large. However, finite element analysis using plate elements can be implemented to evaluate strain energy release rates for debonds at the skin-stiffener interface while requiring many fewer degrees of freedom than are needed for the full 3D analyses.⁷⁻¹⁰ These plate element models, in conjunction with the virtual crack closure technique (VCCT), can be used to evaluate the values for mode I and mode II strain energy release rates accurately. However, several issues arise pertaining to the techniques of modeling debonding with these elements.

The objective of this paper is to quantify the effects of several critical assumptions and parameters on the computation of strain energy release rates for delamination and debond configurations modeled with plate elements. The issues studied are: element order and shear deformation assumptions, constraint of translational degrees of freedom, rotational degrees of freedom or both in the neighborhood of the crack tip, and continuity of material properties and section stiffness in the vicinity of the debond. The discussions that are presented in this paper are pertinent to both delamination and debond analyses for metallic and composite skin-stiffener configurations. In this paper, both an isotropic homogeneous skin and stiffener in a double cantilever beam (DCB) configuration and a composite skin with composite stiffener flanges modeled as homogeneous transversely isotropic materials in a skin-stiffener debond configuration are considered.

Analysis

The skin-stiffener debond configuration and the two simplifying cases that are included in this paper are presented in this section. Next, definitions and procedures used in the literature for the calculation of the strain energy release rates are briefly discussed. Finally, the issues that will be quantified are presented and discussed.

Skin-Stiffener Modeling

A typical composite skin-stiffener configuration with blade stiffeners is shown in Figure 1(a). The configuration and loading are very complex.

* National Research Council

† Head, Mechanics of Materials Branch, Associate Fellow AIAA

Copyright 1998 by the American Institute of Aeronautics and Astronautics, Inc. No copyright is asserted in the United States under Title 17, U.S. Code. The U.S. Government has a royalty-free license to exercise all rights under the copyright claimed herein for Governmental Purposes. All other rights are reserved by the copyright owner

Simplified configurations can be used in these analyses to quantify the effects of the critical assumptions and parameters of interest on the calculation of strain energy release rates. When debonding between the flange and skin takes place along the entire length of the stiffener, a representative portion of the flange and skin can be analyzed as shown in Figures 1(b), 2(a) and 3(a). The double cantilever beam configuration, shown in Figure 2, is a simple configuration which has only mode I loading. The mixed-mode skin-flange debond configuration, shown in Figure 3, has combined mode I and mode II loading. These two configurations are utilized in this paper.

The debonds are modeled with 2D plane strain finite elements (Figure 2(b)) and with non shear-deformable and shear-deformable plate elements (Figures 2(c), 3(b), respectively). Results from the plane strain analyses, which account for shear deformation, will be used as a baseline for comparison with the plate element results. The influence of modeling shear deformation on calculated strain energy release rates can be illustrated by comparing results from the plate element models with those from the plane strain analyses.

In all of the plate finite element models considered herein, the skin and the stiffener are modeled as separate, flat plates. Conventional plate modeling inherently assumes that the reference surface of the plate coincides with the middle surface. Thus, the skin and stiffener are usually modeled by plate elements with nodes at their respective mid-planes. This conventional method is not convenient for modeling debonding because it entails complex constraints to tie the flange nodes to the corresponding skin nodes. A more convenient approach, taken in the present analysis, is to place the skin nodes and the stiffener nodes along the interface between the skin and the stiffener. The positioning of these nodes at the interface is performed by defining an offset distance from the mid-plane of both the skin and the stiffener (see References 9 and 10), as shown in Figure 4.

Strain Energy Release Rates

Figure 5 shows an edge crack of length a in a large plate of unit thickness. The strain energy release rate, G , for self-similar crack growth under constant load is defined as¹¹

$$G = \frac{\partial W}{\partial A} - \frac{\partial U}{\partial A} \quad (1)$$

where U is the total strain energy of the body, W is the external work done on the body and A is the crack surface area.

2D Analysis

To calculate strain energy release rates, G , Irwin proposed the virtual crack closure technique (VCCT)¹². Here, G is calculated by considering the work required to close the crack from $a+\Delta$ to a (see Figure 5(a)). Energy release rate can be separated into mode I and mode II components and calculated by

$$\begin{aligned} G_I &= \lim_{\Delta \rightarrow 0} \left\{ \frac{-1}{2\Delta} \int_0^{\Delta} \sigma_y(x) v(\Delta - x) dx \right\} \\ G_{II} &= \lim_{\Delta \rightarrow 0} \left\{ \frac{-1}{2\Delta} \int_0^{\Delta} \sigma_{xy}(x) u(\Delta - x) dx \right\} \\ G_{Total} &= G_I + G_{II} \end{aligned} \quad (2)$$

where v and u are the crack opening and sliding displacements, respectively, and σ_y and σ_{xy} are the normal and shear stresses ahead of the crack tip. Several methods are available to calculate the strain energy release rates from a single finite element solution using nodal forces ahead of the crack and the crack opening displacements behind the crack.¹³⁻¹⁴

3D Analysis

The VCCT can also be applied to 3D configurations such as the one shown in Figure 5(b). Here, G can be separated into mode I, mode II and mode III components by

$$\begin{aligned} G_I &= \lim_{\Delta \rightarrow 0} \left\{ \frac{-1}{2\Delta \delta z} \int_z^{z+\delta z} \left[\int_0^{\Delta} \sigma_y(x, 0, z) v(\Delta - x, 0, z) dx \right] dz \right\} \\ G_{II} &= \lim_{\Delta \rightarrow 0} \left\{ \frac{-1}{2\Delta \delta z} \int_z^{z+\delta z} \left[\int_0^{\Delta} \sigma_{xy}(x, 0, z) u(\Delta - x, 0, z) dx \right] dz \right\} \\ G_{III} &= \lim_{\Delta \rightarrow 0} \left\{ \frac{-1}{2\Delta \delta z} \int_z^{z+\delta z} \left[\int_0^{\Delta} \sigma_{yz}(x, 0, z) w(\Delta - x, 0, z) dx \right] dz \right\} \\ G_{Total} &= G_I + G_{II} + G_{III} \end{aligned} \quad (3)$$

where u , v and w are the crack face displacements, and σ_y , σ_{xy} and σ_{yz} are the corresponding normal and shear stresses ahead of the crack tip.

The VCCT has been implemented in three-dimensional finite element analyses, where the region near the crack tip is modeled by either eight or twenty-noded brick elements.⁸ As in two-dimensional analysis, the individual mode strain energy release rates can be calculated from the nodal forces and displacements near the crack tip obtained from a single finite element analysis.

Issues

Details of a method for the calculation of strain energy release rate for debond problems using plate elements are given by Wang and Raju.⁹⁻¹⁰ In this method of modeling debonding with plate elements, several critical assumptions are made regarding the effects of

- constraint of translational degrees of freedom, rotational degrees of freedom or both in the neighborhood of the crack tip,
- assumed shear deformation, and
- continuity of material properties and section stiffness in the vicinity of the debond front,

on the values of strain energy release rate computed using the virtual crack closure technique. The effects of each of these assumptions are discussed below. The first two assumptions are discussed in the context of the response of isotropic double cantilever beams, while the last assumption is discussed through analyses of composite orthotropic debond configurations.

Nodal Constraint

Strain energy release rate for debond configurations modeled as plates (Figure 6(a)) can be calculated by means of the virtual crack closure technique from the work required to close the debond from $a+\Delta$ to a . Referring to Figure 6(b), this work term can be computed from the nodal forces (F) and moments (M) at nodes i and i' , and the relative displacements (u , v , w , θ_x , θ_y , θ_z) between nodes p and p' . If each of the six displacement and traction components make a contribution to the energy associated with crack growth, then the formulae for computing the strain energy release rate for an orthogonal and symmetric mesh of 4-noded assumed natural coordinate strain (ANS) plate elements about the crack front are given by

$$G_I = -\frac{1}{2\Delta b_{eq}} \left[F_{zi}(w_p - w_{p'}) + M_{xi}(\theta_{xp} - \theta_{xp'}) \right] \quad (4)$$

$$G_{II} = -\frac{1}{2\Delta b_{eq}} [F_{xi}(u_p - u_{p'})]$$

$$G_{III} = -\frac{1}{2\Delta b_{eq}} [F_{yi}(v_p - v_{p'}) + M_{zi}(\theta_{zp} - \theta_{zp'})]$$

$$G_{Total} = G_I + G_{II} + G_{III}$$

where

$$b_{eq} = \frac{1}{2} [b_{J-1} + b_J]$$

with b_{J-1} and b_J being the width of the $(J-1)^{th}$ and J^{th} strips (see Figure 6) and b_{eq} being the equivalent width apportioned to node i .

If the rotational constraints are applied to paired nodes (e.g., i and i'), then the moments will be nonzero as in Eq. 4. Conversely, if there are no rotational constraints ahead of the crack then the moments are zero and Eq. 4 simplifies to Eq. 5.

$$\begin{aligned} G_I &= -\frac{1}{2\Delta b_{eq}} [F_{zi}(w_p - w_{p'})] \\ G_{II} &= -\frac{1}{2\Delta b_{eq}} [F_{xi}(u_p - u_{p'})] \\ G_{III} &= -\frac{1}{2\Delta b_{eq}} [F_{yi}(v_p - v_{p'})] \end{aligned} \quad (5)$$

Equations 4 and 5 correspond to "Technique-A" and "Technique-B," respectively, in Refs. 9,10. In these references, Technique-B was shown to be the proper modeling technique through comparison to 2D plane strain analyses. Similar equations for 9-noded ANS plate elements that account for the contribution from the midside and midface nodes were presented in reference 7. In a later section of this text, additional justification and insight for this methodology is brought forward.

Shear Deformation of the Elements

Plate elements have been developed extensively since their inception in the 1960's.¹⁵⁻¹⁶ In the present discussion, 4-noded ANS plate elements with no shear deformation and 9-noded ANS plate elements with first order shear deformation are considered. Energy release rate from analyses with both of these plate elements are compared with values from 2D plane strain analyses.

Continuity of Material and Section Properties

The oscillatory singularity near the tip of a crack at a bimaterial interface is a well known artifact of linear elastic fracture mechanics calculations.¹⁷⁻²² The individual modes of the strain energy release rate calculated from finite element analyses do not converge with increasing mesh refinement for the interface crack, although the total strain energy release rate does converge rapidly with mesh refinement.²³ This effect is readily seen in finite element analyses using continuum elements that model the cross-section or in three-dimensional configurational models.²³

In the plate element analyses, details of the cross-section are replaced with prescribed section properties. The configuration shown in Figure 3(a) is used to examine the convergence of the components of the strain energy release rate. The effect of dissimilarities of the material and cross-sectional configuration of the skin and stiffener flange on convergence is discussed.

Results and Discussion

The effects of shear deformation, rotational constraint and continuity of material properties on the computed value of strain energy release rate are presented and discussed in this section. First, the DCB configuration shown in Figure 2(a) is used to illustrate the effects of assumed shear deformation and local rotational and midside node translational constraint. Next, the simplified stiffener debond configuration shown in Figure 3(a) is used to illustrate the effects of section continuity.

A 2D plane strain finite element code, FRANC2D²⁴, and a shell finite element code, STAGS²⁵, were used in these analyses. The FRANC2D model uses quadratic triangular and quadrilateral elements with a rosette of quarter-point triangles at the crack tip. The STAGS v. 2.3 element library includes two elements that are candidates for modeling the debond configurations shown in Figures 2 and 3: a linear displacement shell having no shear deformation and a quadratic Lagrangian shell that includes first order shear deformations.

DCB Configuration: Shear Deformation and Nodal Restraint

A DCB configuration, as shown in Figure 2(a), with $l=1.0$ in., $a=0.25$ in. and $h=0.025$ in. was analyzed. The applied load is entirely shear, Q , with a magnitude of 1.0 lb./in. The material was assumed to be isotropic and homogeneous with a Young's modulus of 10.0×10^6 psi and a Poisson's ratio of 0.30 . Plane strain solutions were obtained using the finite element code FRANC2D for crack lengths between 0.01 and 0.50 in. for three beam lengths, l . Strain energy release rates calculated in these analyses are shown in Figure 7. The analyses show that the beam length, l , has negligible effect on the strain energy release rates until $a/l=0.8$. Thus, if the crack length is significantly shorter than the length of the beam, the strain energy release rate is only a function of the crack length, a , and the beam thickness, h .

Displacements in the x - and z -directions along vertical sections of the beam are presented in Figure 8. Sections at the crack tip, one plate thickness (h) in front of the crack tip, and two plate thicknesses ($2h$) in front of the crack tip are considered. For the section located at the crack tip, maximum displacements in the x -direction (thick solid line) are larger than the maximum displacements in the z -direction (thick dotted line). Here, displacements in the x -direction are approximately a linear function of position through the thickness. That is, the plate theory assumption that plane sections remain plane is reasonable at the crack tip. Displacements along the

vertical section one thickness in front of the crack tip in both the x -direction (medium solid line) and the z -direction (medium dashed line) are approximately 10% of the corresponding displacements along the vertical section at the crack tip. The displacements along the vertical section two thicknesses in front of the crack tip in the x -direction (fine solid line) and z -direction (fine dashed line) are negligible.

Wang and Raju⁹⁻¹⁰ suggested releasing the rotational degrees of freedom in front of the crack tip in plate or shell analyses of debond problems to allow deformations in the x -direction similar to those shown in Figure 8. This methodology resulted in accurate energy release rate calculations for debond problems using plate elements. In this paper, five different methods of modeling near-crack tip deformations are considered. These methods use two different elements, and constrain different degrees of freedom ahead of the crack tip, as summarized in Table 1 and Figure 9. The ability of these methods to model near-crack tip deformations (such as those shown in Figure 8) accurately has a significant effect on the accuracy of the energy release rate calculations.

Table 1 Plate Element Modeling Methods

Method	Shear Deformable Element	DOF Restrained
1	Yes	$w _{\text{all nodes}}$
2	Yes	$w _{\text{edge nodes}}$
3	Yes	$w, \theta_y _{\text{all nodes}}$
4	No	$w _{\text{all nodes}}$
5	No	$w, \theta_y _{\text{all nodes}}$

Figure 10 is a plot of G vs. a using the five methods discussed previously, as well as the baseline plane strain solution. For the range of crack lengths of $0.0 < (a/h) < 10.0$, both Method 1 and Method 2 approximate the plane strain solution well. Method 3 underpredicts G values by about 5% to 10%. Method 4 and Method 5, which do not account for shear deformation, underpredict G values by approximately 50%.

Figure 11 shows the convergence characteristics of strain energy release rate calculated by Methods 1-5. A comparison of the converged values, predicted with the plate element methods, to the plane strain solution illustrates the need for proper modeling of shear deformation. The deformation shown in Figure 8 is an essential aspect of the near crack tip deformation field that cannot be modeled properly by plate elements that do not allow shear deformations. Methods 4 and 5 do not allow for shear deformation anywhere in the model, and do not predict energy release rates accurately. Method 3 has rotations restrained to be zero at and ahead of the crack tip, but

allows for shear deformations behind the crack tip. As a result, the model is overly stiff, but predicts energy release rates much closer to the plane strain values than are predicted by Methods 4 and 5. Both Methods 1 and 2 allow for rotations due to shear deformation ahead of and behind the crack tip. The converged values of energy release rate for both of these methods approach the same value and are within three percent of the plane strain value.

As shown in Figure 11, Method 1 and Method 2 converge to the same value, which agrees well with the plane strain value of G . However, Method 1 converges from below while Method 2 converges from above when compared with the plane strain value of G . The element midside nodes in front of the crack tip in Method 1 (see Figure 9) are restrained against vertical displacements, whereas the same nodes in models corresponding to Method 2 are allowed to displace freely. Since Method 1 requires that each element in front of the crack tip has vertical nodal translations restrained, there can be no vertical displacement at any point in the element. Conversely, Method 2 relaxes the constraint by requiring that each element in front of the crack tip has restrained vertical nodal translations only at the edge nodes as shown in Figure 9.

For any degree of mesh refinement, Method 2 allows two types of displacement to occur in front of the crack tip: translations and rotations due to both bending and shear. Thus, Method 2 is overly compliant. As the mesh refinement increases, the distance between restrained end nodes of each element decreases, and the deformations in front of the crack tip become dominated by shear. In contrast, Method 1 has the midside and midface nodes restrained in the vertical direction. This constraint disallows the bending deformation shown in Figure 8, causing shear to be the dominant mode of deformation in front of the crack tip for any degree of mesh refinement using this method.

Debond Configuration: Continuity

In this section, issues of continuity associated with complicated structures such as the one shown in Figure 1 are addressed. For the purposes of

illustration, the skin is assumed to be constructed of unidirectional graphite/epoxy plies with properties⁹⁻¹⁰

$$\begin{aligned} E_{11} &= 19.5 \times 10^6 \text{ psi} & E_{22} &= E_{33} = 1.48 \times 10^6 \text{ psi} \\ \mu_{12} &= \mu_{13} = 0.80 \times 10^{-6} \text{ psi} & \mu_{23} &= 0.497 \times 10^{-6} \text{ psi} \\ \nu_{12} &= \nu_{13} = 0.30 & \nu_{23} &= 0.49 \end{aligned}$$

where E_{ij} , μ_{ij} , ν_{ij} ($i, j=1,2,3$) are the Young's moduli, shear moduli, and Poisson's ratio, respectively, and the subscripts 1,2,3 represent the fiber and two transverse directions, respectively.

The oscillatory singularity is an artifact of elastic modeling of cracks at bimaterial interfaces.¹⁷⁻²² Attempts to eliminate this artifact in two-dimensional and three-dimensional continuum analyses are reported in the literature²⁶ and are not discussed here. Rather, the present discussion is an effort to present the effects of continuity on strain energy release rate analyses based on plate elements.

Figure 3 shows the general configuration that will be used to illustrate the effect of material and stiffness continuity on the convergence of strain energy release rate. Here, $l_1 = 1.0$ in., $l_2 = 1.0$ in. and $a = 0.40$ in. The applied load is entirely shear, Q , with a magnitude of 1.0 lb./in. Cylindrical bending boundary conditions were applied to the model as shown in Figure 3(a). Table 2 gives the skin and flange thicknesses and layups for each of the five configurations examined herein. In the analyses that follow, the shear deformable quadratic element with prescribed zero z -direction translations at all nodes, corresponding to Method 1 in the previous section, is used. Strain energy release rates are computed using Eq. 5. The reasons for examining these configurations were to study the effects of material and geometric section property continuity on the convergence of strain energy release rate with decreasing element size for structures modeled with plate elements.

Figures 12-16 show the change in the computed values of G_I , G_{II} and G_{Total} as a function of element size. Configuration 1 is a configuration with the skin and flange of the same thickness and layup, *i.e.* with identical extensional, shear and bending stiffnesses. In Figure 12 (Configuration 1), both the total and the individual modes of strain energy release rate are well

Table 2 Skin-Flange Configurations

Configuration	Flange Thickness (inches)	Flange Layup	Skin Thickness (inches)	Skin Layup	Plies at Interface
1	0.20	[0] ₄₀	0.20	[0] ₄₀	0/0
2	0.20	[0 ₂₀ /90 ₂₀]	0.20	[0] ₄₀	90/0
3	0.20	[0 ₂₀ /90 ₂₀]	0.20	[0 ₂₀ /90 ₂₀]	90/0
4	0.20	[0 ₁₀ /90 ₂₀ /0 ₁₀]	0.20	[0] ₄₀	0/0
5	0.10	[0] ₂₀	0.20	[0] ₄₀	0/0

behaved and converge for even very large element sizes approaching 10% of the length ($l_1 + l_2$ in Figure 3(a)).

Figures 13-16 show the computed values of G_I , G_{II} and G_{Total} as a function of element size for Configurations 2-5, respectively. As seen in the figures, the total strain energy release rate is well behaved and converged for even large element sizes. However, over the range of element sizes considered, the individual modes continue to change regardless of element size for each of these cases.

Configuration 2, shown in Figure 13, has a skin and flange with the same thickness, but with an unsymmetric layout in the flange. Thus, the flange has different extension, shear and bending stiffnesses than the skin. In addition, the flange exhibits extension-bending coupling.²⁷ The individual effects of having different skin and stiffener stiffnesses and extension-bending coupling can be examined by considering Configurations 3 and 4, respectively. Figure 14 shows the results for Configuration 3 whereupon the skin and flange are both unsymmetric. Although they both have identical extension, shear and bending stiffnesses, the modes continue to change throughout the range of element sizes considered. Thus, extension-bending coupling alone is sufficient to inhibit convergence of the individual modes over this broad range of element sizes. Figure 15 shows the strain energy release rate for Configuration 4, where the skin and flange have the same thickness. Although the flange is symmetric and has no extension-bending coupling, it has different extension, shear and bending stiffnesses than the skin. Thus, different stiffness for the skin and flange alone is sufficient to inhibit convergence of the individual modes. Finally, Figure 16 shows the results for Configuration 5 whereupon the skin and flange have the same layout, but different thicknesses. This configuration is similar to Configuration 4 in that the skin and flange have different stiffness with no coupling. Again, the modes change over the range of element sizes that were considered.

Concluding Remarks

The effects of several critical assumptions and parameters on the computation of strain energy release rates for delamination and debond configurations modeled with plate elements have been quantified. The issues studied are: element order and assumed shear deformation, constraint of translational degrees of freedom, rotational degrees of freedom or both in the neighborhood of the crack tip, and continuity of material properties and section stiffness in the vicinity of the debond. The discussions that were presented in this paper are pertinent to both delamination and

debond analyses for metallic and composite skin-stiffener configurations.

The analyses suggest that properly accounting for the effects of shear deformation and assumed compatibility are critical when computing the strain energy release rates with the virtual crack closure technique (VCCT) applied to plate elements. Five methods for implementing plate elements in these calculations were considered. The method in which shear deformation was considered and vertical nodal translations were restrained at all nodes ahead of the crack tip is the preferable method because it most rapidly converges to the plane strain solutions.

The results of the simulations of the debond configurations with discontinuous section properties suggest that some or all of the characteristics of the classical bimaterial interface problem can be present when modeling with this plate element-based technique. In the plate element models, the section properties depend on both material and geometric properties. When the section properties above and below the crack plane are discontinuous, the total strain energy release rate is well behaved, but the modes do not converge or converge very slowly. Conversely, when the section properties are continuous, both the total strain energy release rate and the individual modes are well behaved.

Acknowledgments

The authors wish to thank Drs. T.W. Coats, C.C. Rankin, J.T. Wang and R.D. Young for many helpful comments during the course of this work. This research was performed while two of the authors (EHG, WTR) were National Research Council Research Associates in the Mechanics of Materials Branch of NASA Langley Research Center.

References

1. Wang, J.T.S. and Biggers, S.B., "Skin/Stiffener Interface Stresses in Composite Stiffened Panels," NASA CR 172261, 1984.
2. Hyer, M.W. and Cohen, D., "Calculation of Stresses and Forces Between the Skin and Stiffener in Composite Panels," *28th AIAA/ASME/ASCE/AHS Structures, Structural Dynamics and Materials Conference*, AIAA Paper 87-0731-CP, 1987.
3. Cohen, D. and Hyer, M.W., "Influence of Geometric Nonlinearities on Skin-Stiffener Interface Stresses," *29th AIAA/ASME/ASCE/AHS Structures, Structural Dynamics and Materials Conference*, AIAA Paper 88-2217-CP, 1988.

4. O'Brien, T.K., "Characterization of Delamination Onset and Growth in a Composite Laminate," *Damage in Composite Materials, ASTM STP 775*, 1982, pp. 140-167.
5. Wang, A.S.D. and Crossman, F.W., "Initiation and Growth of Transverse Cracks and Edge Delamination in Composite Laminates, Part 1: An energy method," *Journal of Composite Materials*, Vol. 14, 1980, pp. 71-87.
6. Whitcomb, J.D., "Instability-Related Delamination Growth of Embedded and Edge Delaminations," *NASA TM 100655*, 1988.
7. Wang, J.T., Raju, I.S., and Sleight, D.W., "Composite Skin Stiffener Debond Analyses Using Fracture Mechanics Approach with Shell Elements," *Composites Engineering*, Vol. 5, No. 2, 1995, pp. 277-296.
8. Raju, I.S., Sistla, R. and Krishnamurthy, T., "Fracture Mechanics Analyses for Skin-Stiffener Debonding," *Engineering Fracture Mechanics*, Vol. 54, No. 3, 1996, pp. 371-385.
9. Wang, J.T., Raju, I.S., Davila, C.G. and Sleight, D.W., "Computation of Strain Energy Release Rates for Skin-Stiffener Debonds Modeled with Plate Elements," 34th AIAA/ASME/ASCE/AHS Structures, Structural Dynamics and Materials Conference, AIAA Paper 93-1501-CP, 1993, pp. 1680-1692.
10. Wang, J.T. and Raju, I.S., "Strain Energy Release Rate Formulae for Skin-Stiffener Debond Modeled with Plate Elements," *Engineering Fracture Mechanics*, Vol. 54, No. 2, 1996, pp. 211-228.
11. Broek, D., *Elementary Engineering Fracture Mechanics*, 4th Edition, Martinus Nijhoff, Boston, MA, 1987.
12. Irwin, G.R., "Fracture," *In Handbuch der Physik*, Vol. 6, 1958, pp. 551.
13. Rybicki, E.F. and Kanninen, M.F., "A Finite Element Calculation of Stress Intensity Factors by a Modified Crack Closure Integral," *Engineering Fracture Mechanics*, Vol. 9, 1977, pp. 931-938.
14. Raju, I.S., "Calculation of Strain-Energy Release Rates with Higher Order and Singular Finite Elements," *Engineering Fracture Mechanics*, Vol. 28, No. 3, 1987, pp. 251-274.
15. Cook, R.D., Malkus, D.S., Plesha, M.E., *Concepts and Applications of Finite Element Analysis*, 3rd Edition, Wiley, New York, 1989.
16. Hrabok, M.M. and Hrudey, T.M., "A Review and Catalog of Plate Bending Finite Elements," *Computers and Structures*, Vol. 19, No. 3, 1984, pp. 479-495.
17. Williams, M.L., "The Stresses Around a Fault or Crack in Dissimilar Media," *Bull. Seismol. Soc. Am.*, Vol. 49, 1959, pp. 199-204.
18. Erdogan, F., "Stress Distribution in Bonded Dissimilar Materials with Cracks," *Journal of Applied Mechanics*, Vol. 32, 1965, pp. 403-410.
19. Rice, J.R. and Sih, G.C., "Plane Problems of Cracks in Dissimilar Media," *Journal of Applied Mechanics*, Vol. 32, 1965, pp. 418-423.
20. Rice, J.R., "Elastic Fracture Mechanics Concepts for Interface Cracks," *Journal of Applied Mechanics*, Vol. 55, 1988, pp. 98-103.
21. Comninou, M., "The Interface Crack," *Journal of Applied Mechanics*, Vol. 54, 1987, pp. 828-832.
22. Hutchinson, J.W., Mear, M.E. and Rice, J.R., "Crack Paralleling an Interface Between Dissimilar Materials," *Journal of Applied Mechanics*, Vol. 54, 1987, pp. 828-832.
23. Raju, I.S., Crews Jr., J.H. and Aminpour, M.A., "Convergence of Strain Energy Release Rate Components for Edge-Delaminated Composite Laminates," *Engineering Fracture Mechanics*, Vol. 30, No. 3, 1988, pp. 383-396.
24. Wawrzynek, P. and Ingraffea, A., *FRANC2D: A Two-Dimensional Crack Propagation Simulator*, NASA CR-4572, March 1994.
25. Brogan, F.A., Rankin, C.C., Cabiness, H.D. and Loden, W.A., *STAGS User Manual*, Lockheed Martin Missiles and Space Co., July 1996.
26. Raju, I.S. and Dattaguru, B., "Review of Methods for Calculating Fracture Parameters for Interface Crack Problems," *Computational Mechanics 1995: Proceedings of the International Conference on Computational Engineering Science*, S.N. Atluri, G. Yagawa and T.A. Cruise, eds., 1995, pp. 2020-2026.
27. Jones, R.M., *Mechanics of Composite Materials*, Hemisphere Publishing Corporation, New York, 1975.

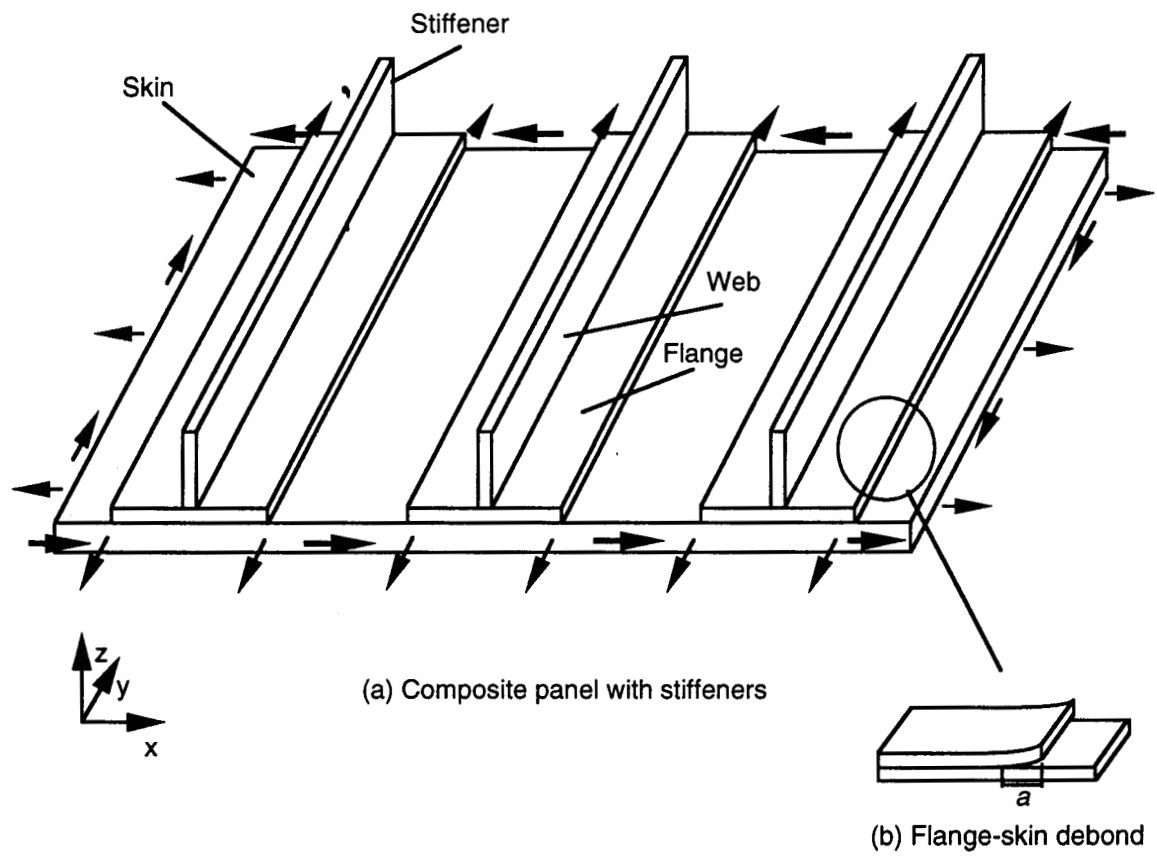
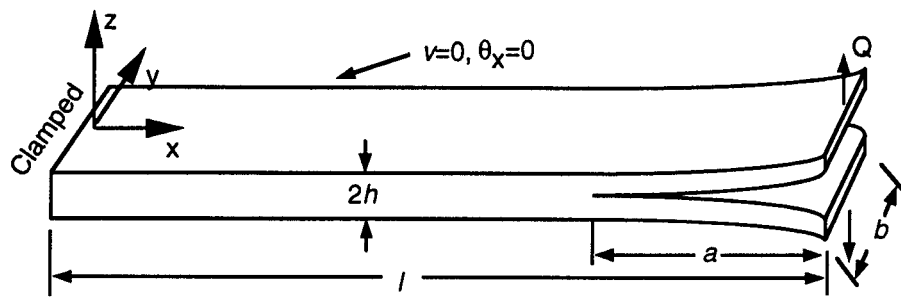
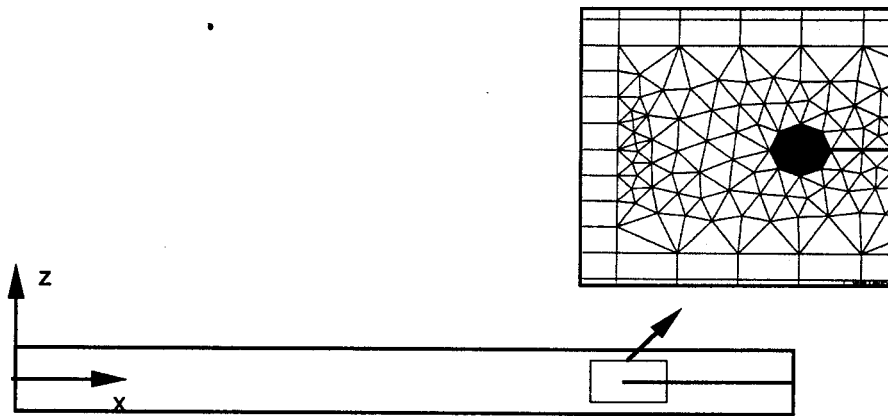


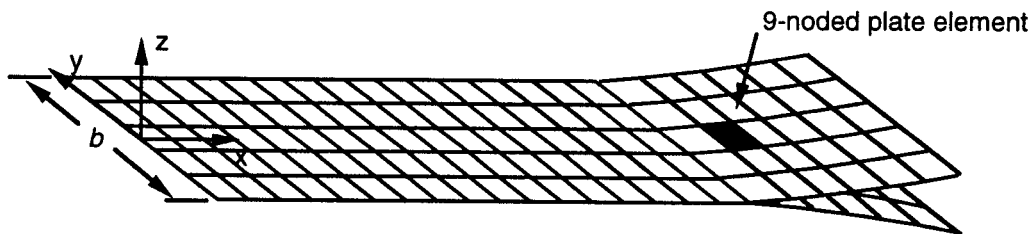
Figure 1 Composite skin-stiffened panel



(a) Double cantilever beam configuration

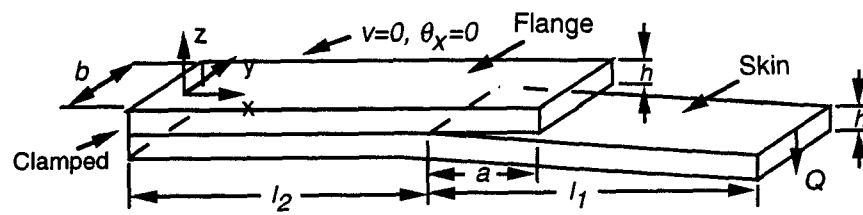


(b) Plane strain model with crack tip detail showing rosette of 6-noded quarter point triangles

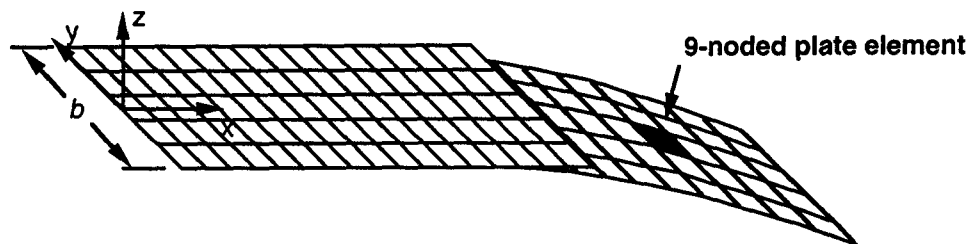


(c) Plate element model - cylindrical bending

Figure 2 Double cantilever beam configuration and models



(a) Flange-skin debond configuration



(b) Plate element model - cylindrical bending

Figure 3 Flange-skin debond configuration and models

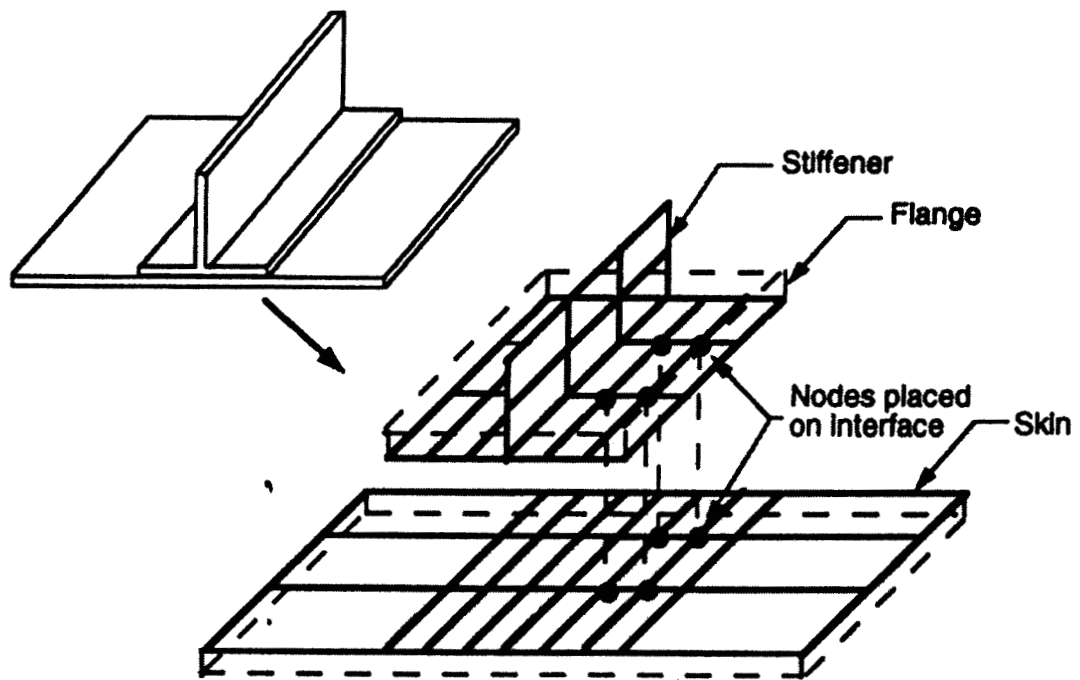


Figure 4 Plate element model of skin and stiffener

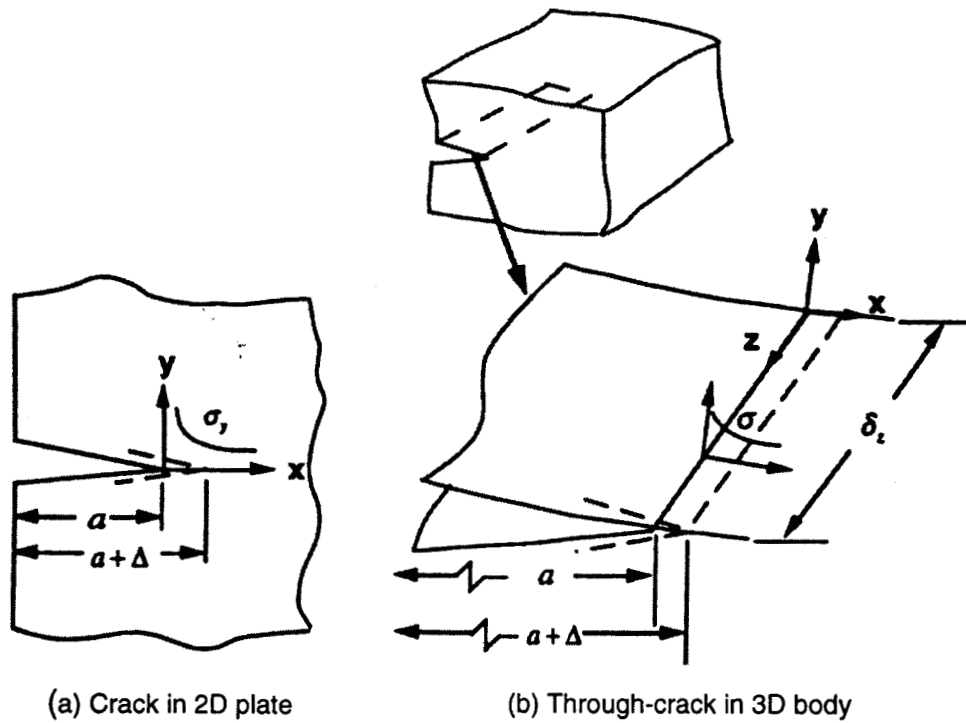
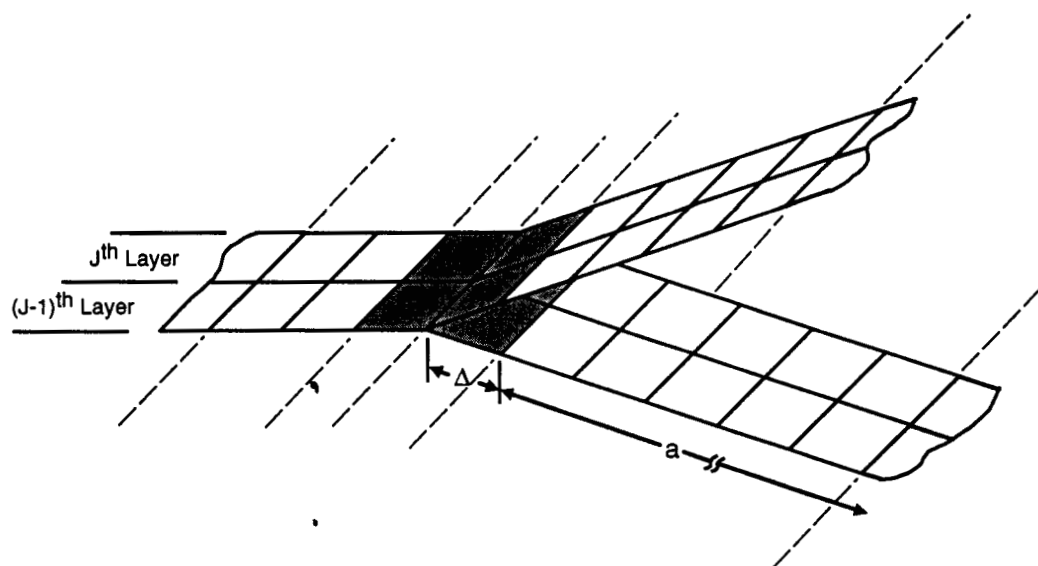
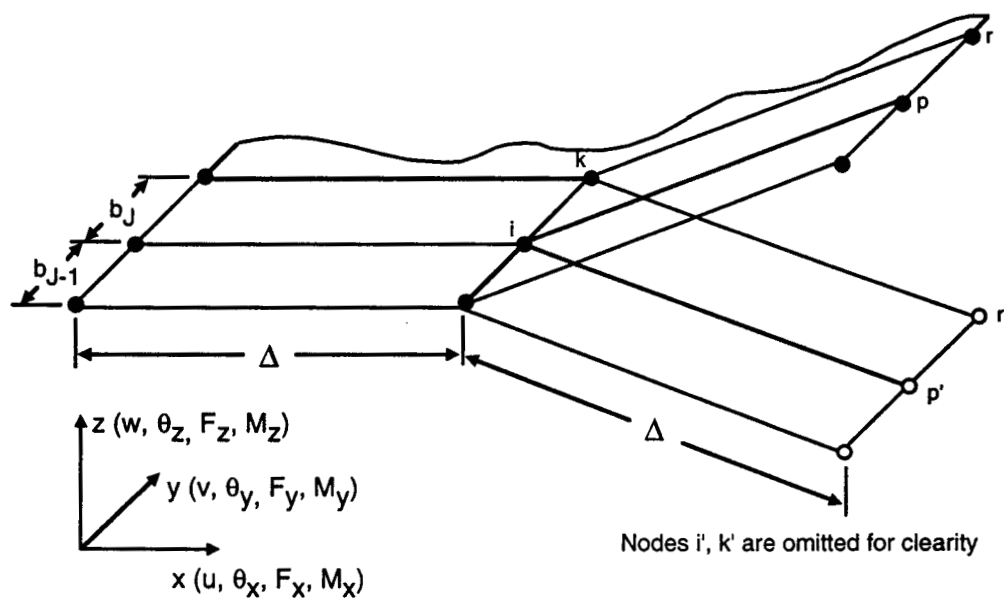


Figure 5 VCCT approach for G-calculation



(a) Plate element modeling near the debond front



(b) Details of the model near the debond front

Figure 6 Debond configuration modeled using 4-node plate elements

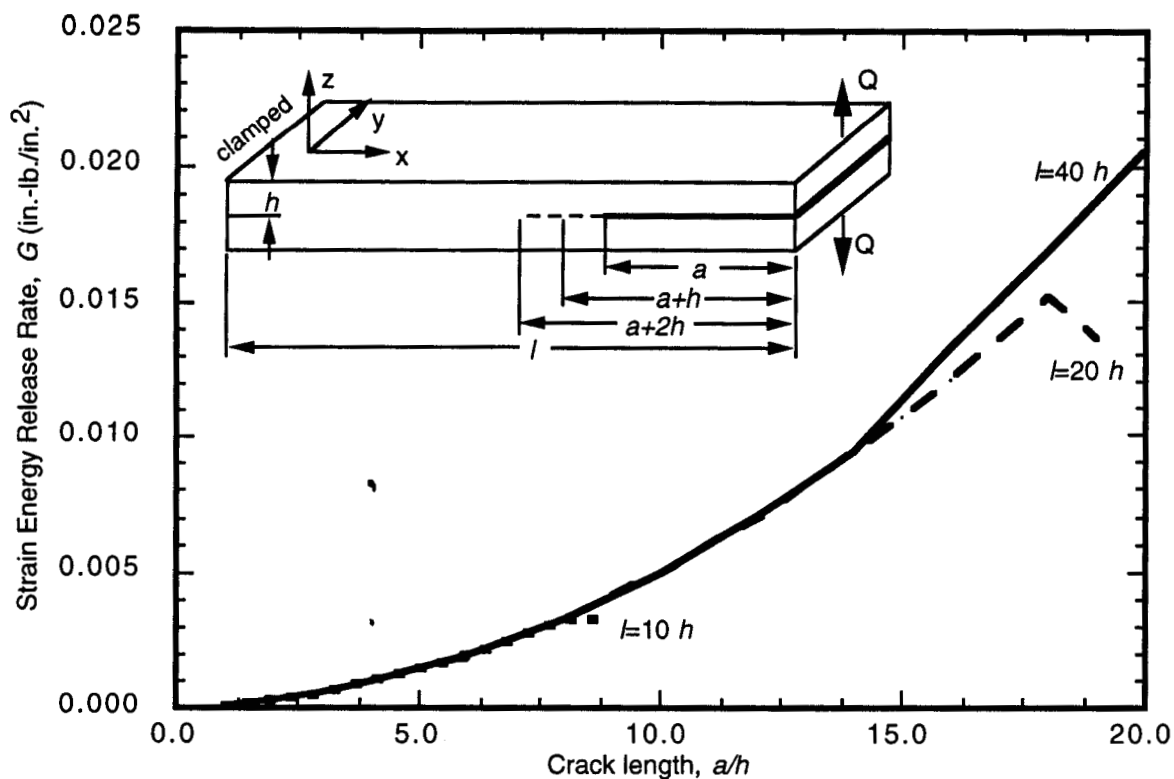


Figure 7 Strain energy release rate for several length beams under unit load

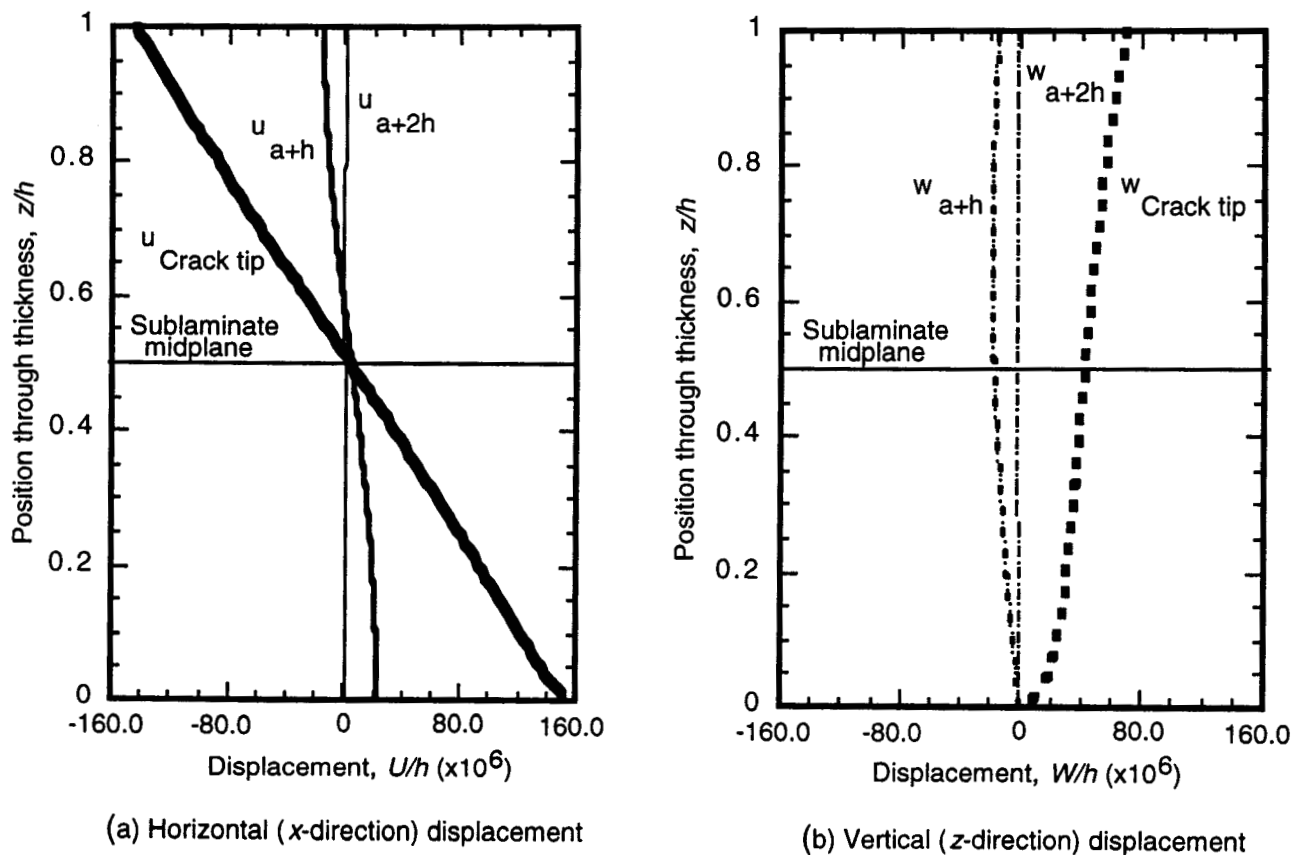


Figure 8 Displacements along three vertical planes near the crack tip

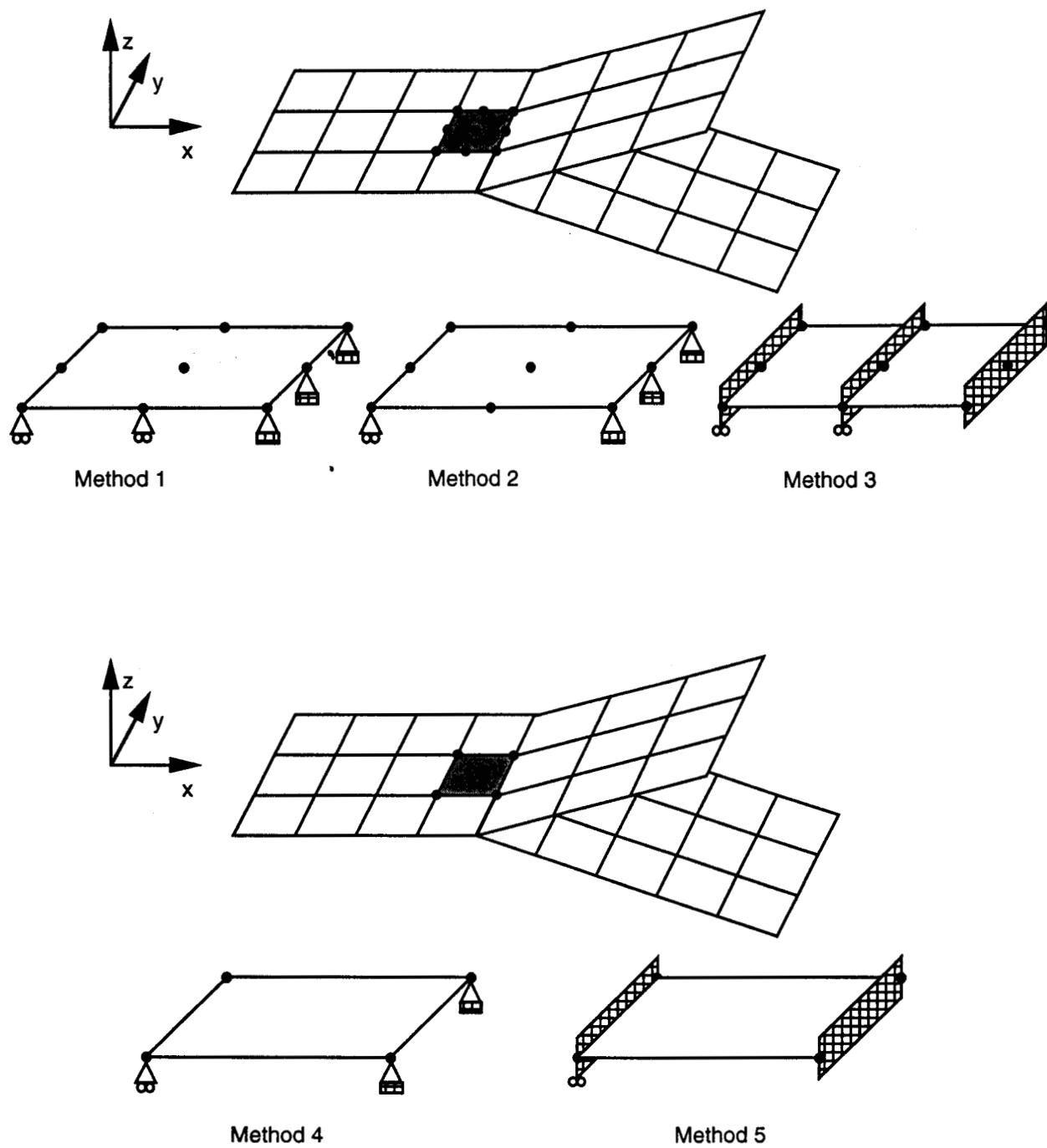


Figure 9 Plate element modeling methods for elements ahead of crack front

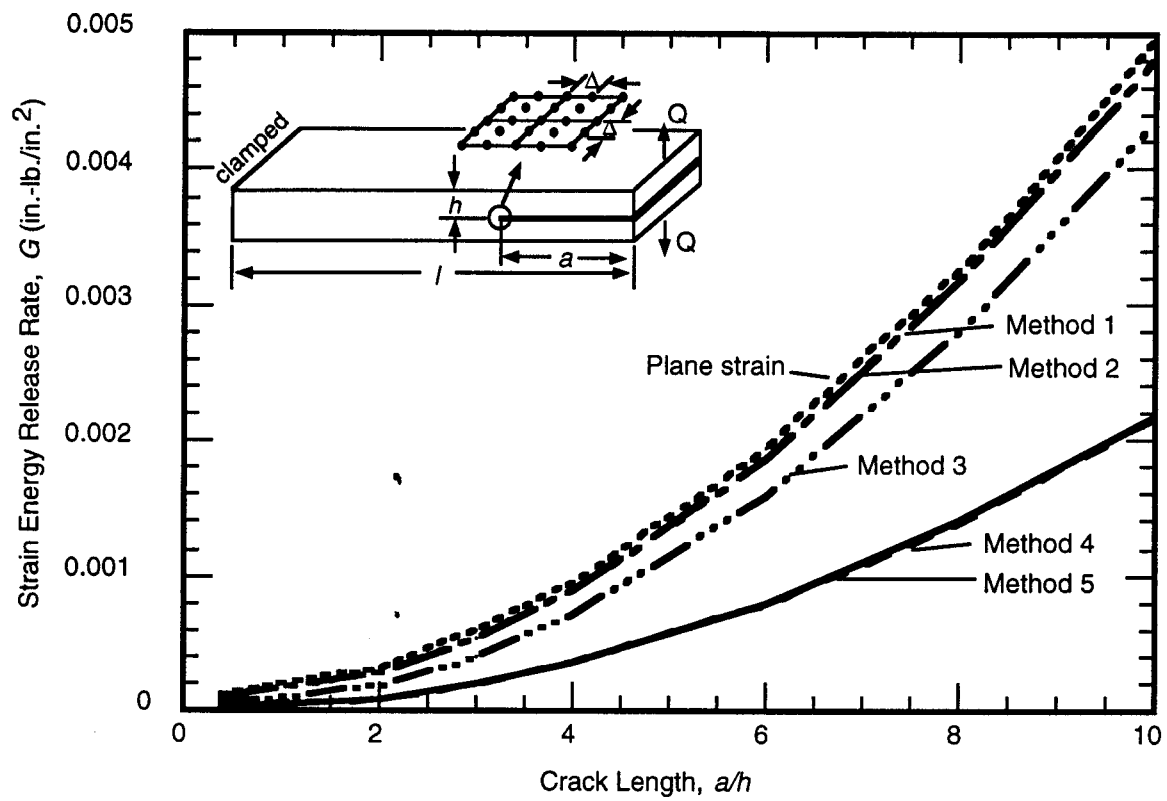


Figure 10 Strain energy release rate for five methods and plane strain ($Q=1.0$ lb./in.)

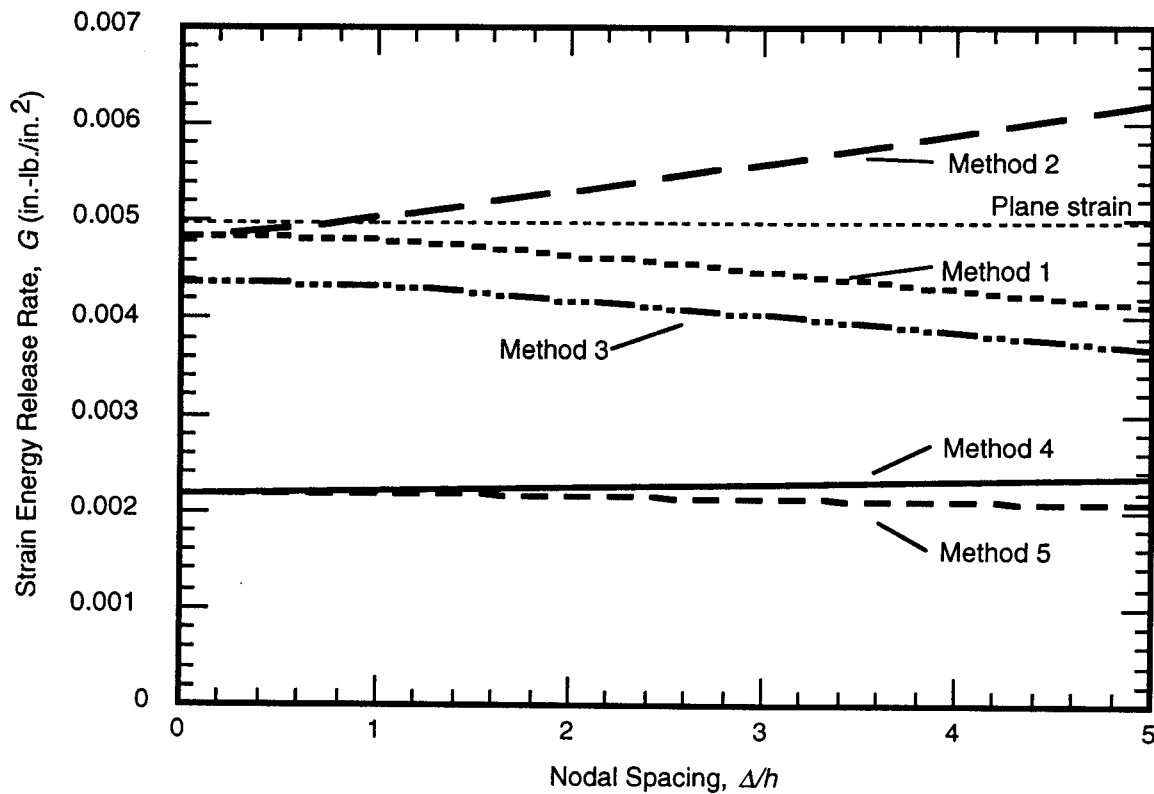


Figure 11 Convergence of strain energy release rate ($a=0.25$, $h=0.025$)

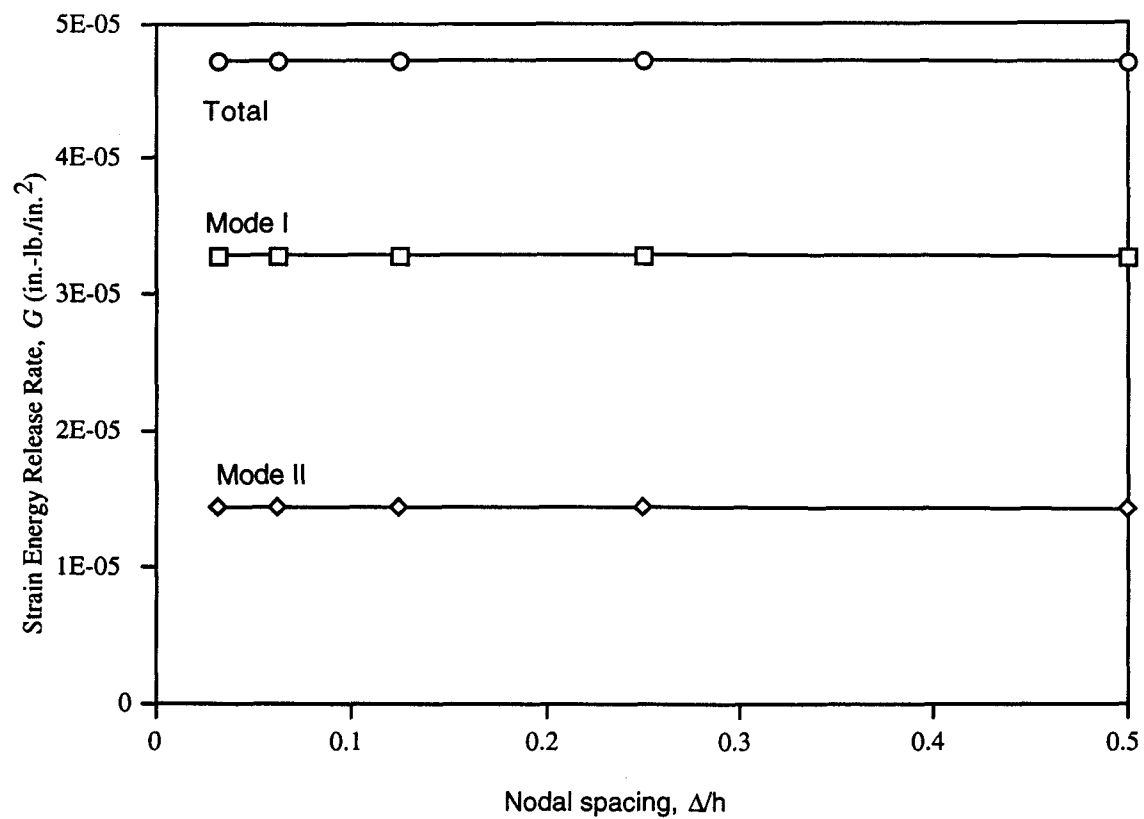
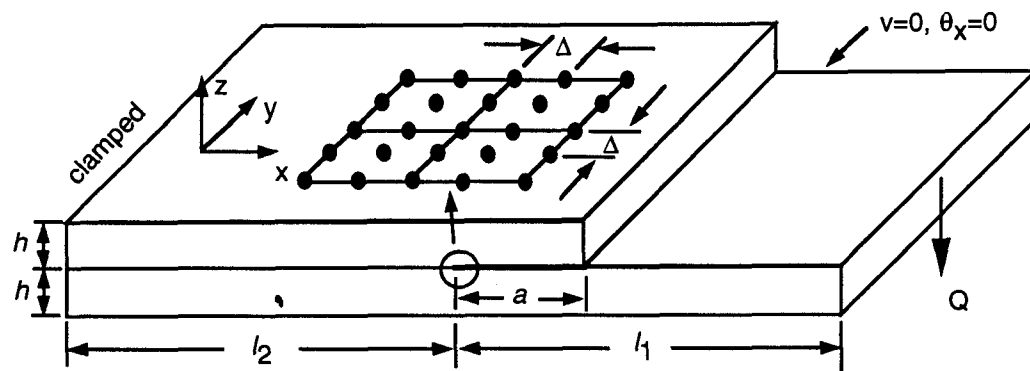


Figure 12 Strain energy release rate for debond configuration with similar flange and skin (Configuration 1)

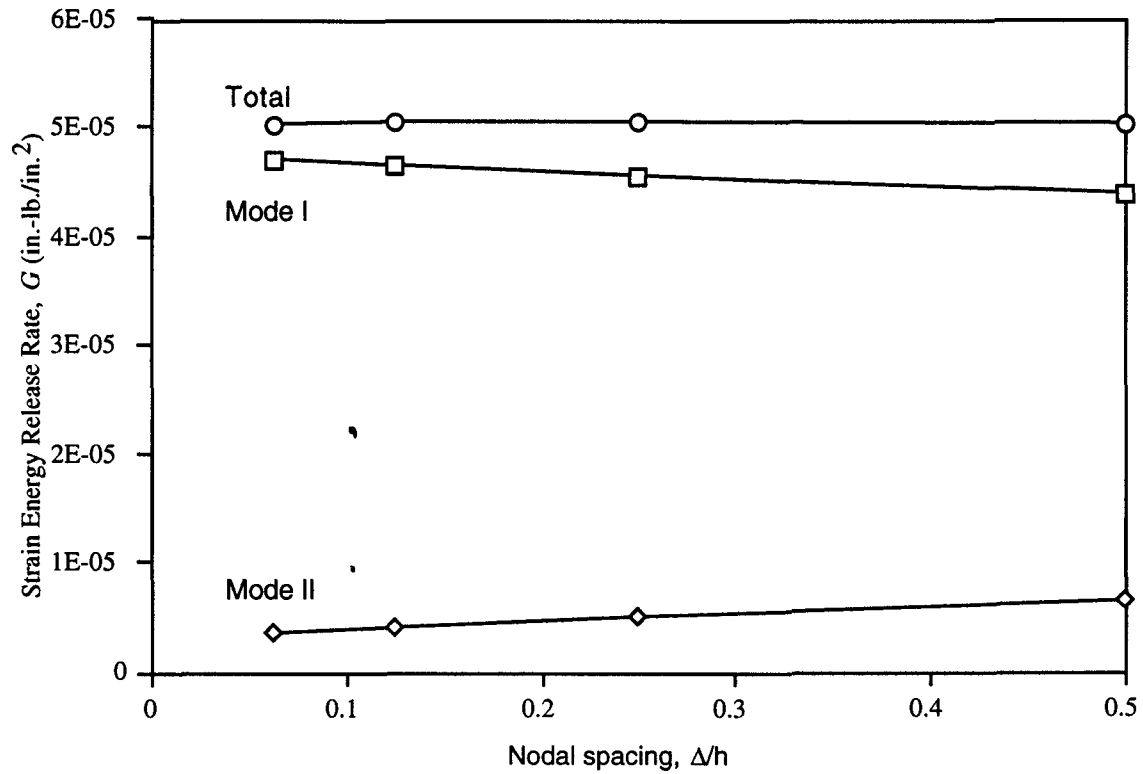


Figure 13 Strain energy release rate for debond configuration with unsymmetric flange (Configuration 2)

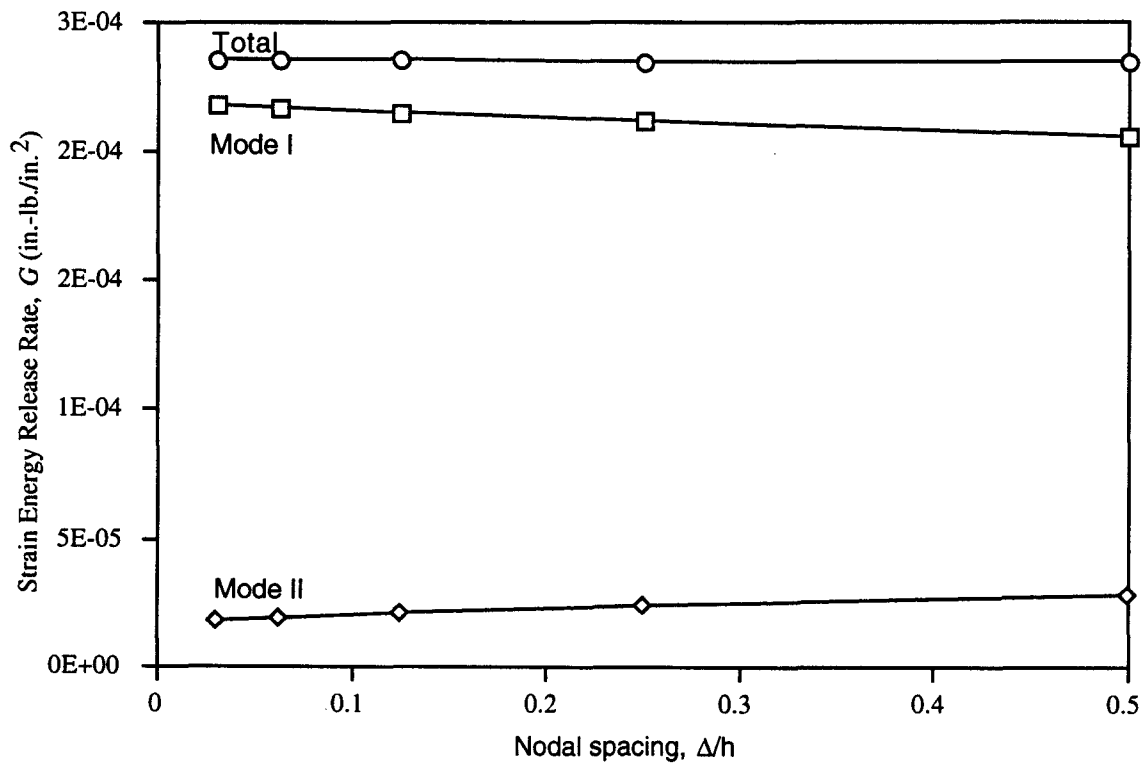


Figure 14 Strain energy release rate for debond configuration with unsymmetric skin and flange (Configuration 3)

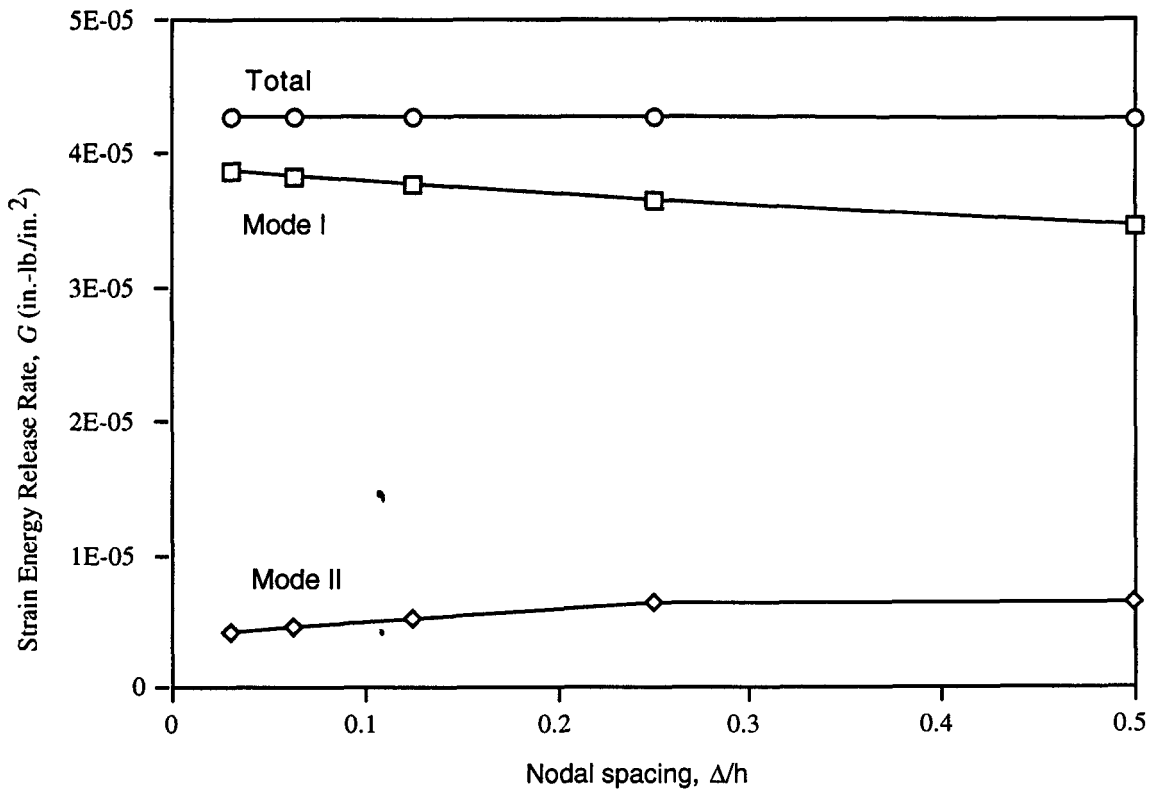


Figure 15 Strain energy release rate for debond configuration with skin and flange with different thickness (Configuration 4)

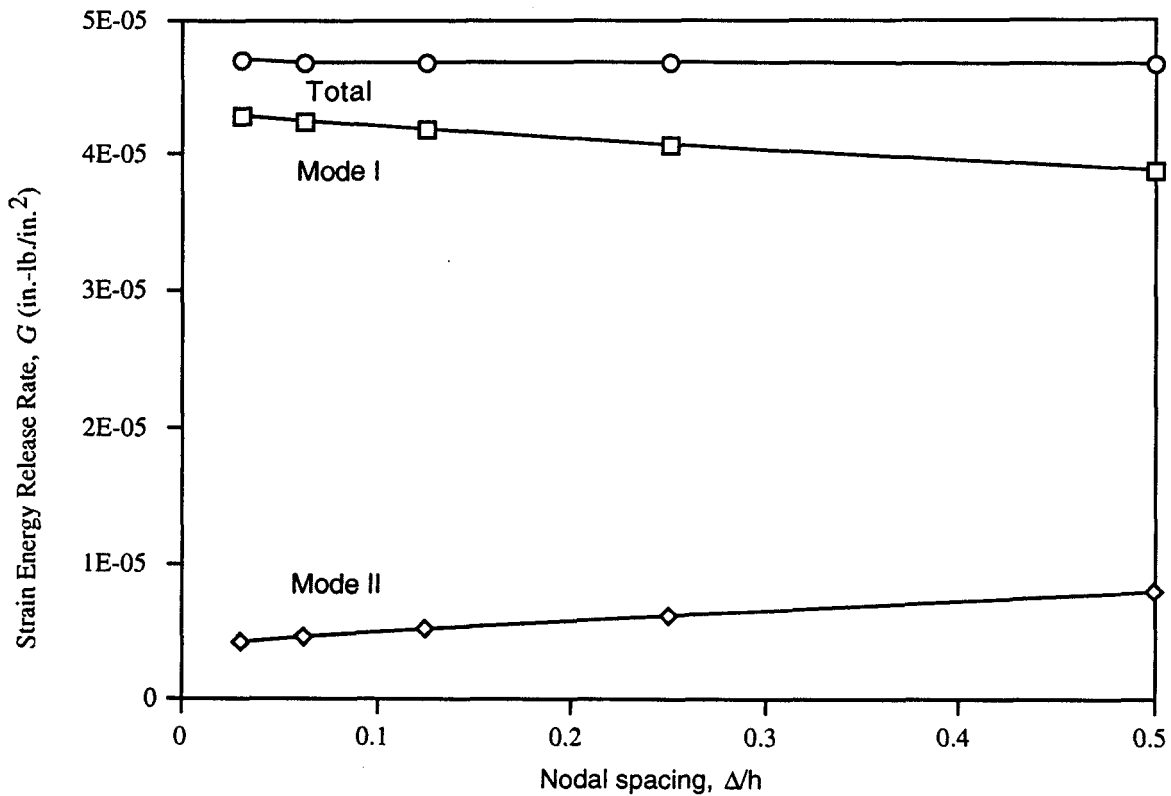


Figure 16 Strain energy release rate for debond configuration with flange with half of the skin thickness (Configuration 5)